Applied Catalysis B: Environment and Energy 361 (2025) 124673

Contents lists available at ScienceDirect

Applied Catalysis B: Environment and Energy

journal homepage: www.elsevier.com/locate/apcatb

Joule heating synthesis for single-atomic Fe sites on porous carbon spheres and armchair-type edge defect engineering dominated oxygen reduction reaction performance

Yifei Liu [a], Lingbo Zong [b,*], Yuanyuan Zhang [b], Fenghong Lu [a], Lei Wang [b,*]

[a] College of Environment and Safety Engineering, Qingdao University of Science and Technology, Qingdao 266042, PR China
[b] College of Chemistry and Molecular Engineering, Qingdao University of Science and Technology, Qingdao 266042, PR China

ARTICLE INFO

Keywords:
Joule heating
Single atom catalyst
Defect
Armchair-type
Oxygen reduction reaction

ABSTRACT

Single-atom catalysts (SACs) embedded in heteroatom-doped carbon are the most promising oxygen reduction reaction (ORR) electrocatalysts. However, the expeditious and facile synthesis of high-performance SACs with Fe-N_x active sites and identifying the role of edge-type defect at the atomic level in carbon support are essential but remain challenging. Herein, Joule heating is applied to anchor Fe single atoms on newly defect rich porous carbon spheres (Fe-N-DCSs) in milliseconds. Fe-N-DCSs achieves exceptional ORR performance, with a half-wave potential ($E_{1/2}$) of 0.90 V and $E_{1/2}$ lost of only 20 mV after 30,000 cycles in 0.1 M KOH, and superior Zn-air batteries performances. Density functional theory calculations establish that armchair-type edge defects decorated Fe-N_4 active sites boost the desorption of OH* and diminish the ORR overpotential. This work not only provides a speedy route for the fabrication of SACs but also presents new insights into the excellent ORR activity.

1. Introduction

The oxygen reduction reaction (ORR) is valuable to the research of fuel cells, metal-air batteries and fundamental electrochemistry studies [1,2]. It is well recognized that Pt catalysts deliver the optimum oxygen binding energy of ORR and show the most efficient ORR performance [3,4]. However, the high cost and poor storage of Pt hinder its widespread application [5,6]. Therefore, it is extremely imperative to prepare non-precious metal catalysts for ORR. Single-atom catalysts (SACs) have attracted tremendous attention because of their highest atom utilization efficiency, and remarkable intrinsic activity, and possess significant research potential in sustainable energy conversion technology [4,7]. Especially, the well-established metals single atoms (SAs) embedded in N-doped carbon (M-N-Cs) with high conductivity, adjustable electronic structures of the active centers, and excellent ORR performance are considered as highly promising alternatives to Pt-based catalysts [8–11]. Early studies testified that porous carbon materials with rich defects are not only ideal platforms to anchor metal atoms but also could decorate the electronic structures of active sites [12,13]. Thus, the ORR activity of metals SAs is support-sensitive. Identification of the exact role of edge-type defect sites in carbon support during ORR is vital for the rational design of catalysts [14]. Currently, the main approach to preparing carbon supports is pyrolytic metal-organic frameworks (MOFs), but their poor stability and high cost impede further development [15–17]. Hence, it is necessary to develop new porous carbon supports with a high content of defects.

The synthesis of SACs successfully is a prerequisite for further studies into their structures, properties and applications [18,19]. Generally, the synthesis approaches of SACs can be summarised into two main categories, top-down and bottom-up strategies [20,21]. For instance, Li et al. stated the successful conversion of noble metal nanoparticles to single atoms by a time-consuming and energy-intensive pyrolysis method under an inert atmosphere [22]. Wu et al. constructed SACs with a tri-nuclear active structure by pyrolysis of Mn ion-adsorbed ZnCo zeolite imidazolite skeleton (ZIF) [23]. Obviously, the universal step of these approaches for yielding SACs is time-consuming [24,25]. However, SAs with high free energy tend to agglomerate to form clusters or nanoparticles during the prolonged high-temperature pyrolysis process, which seriously restricts the precise synthesis of SACs [18,26,27]. Therefore, it is necessary to explore new strategies to synthesize SACs speedily and conveniently. Impressively, Joule heating, attaining the target temperature in milliseconds and instantaneous quenching, can reduce the environmental impact and avoid the loss of favorable N specials [28–30]. As far as we know, research on the synthesis of SACs

---

* Corresponding authors.
E-mail addresses: lingbozong@qust.edu.cn (L. Zong), inorchemwl@126.com (L. Wang).

https://doi.org/10.1016/j.apcatb.2024.124673
Received 15 July 2024; Received in revised form 5 September 2024; Accepted 3 October 2024

simultaneously realizing high activity and longevity using joule heating is scarce and still needs to be further explored [31].

Joule heating, which can rapidly transform electricity into heat, is an innovative and promising method for eco-friendly, high-efficiency and well-controlled chemical synthesis [32]. Joule heating can achieve 3000 K at an extraordinarily rapid rate, breaking the shackles of traditional heating methods [33,34]. Not only can the agglomeration and Ostwald ripening of nanoparticles be avoided, but also new phase structures can be generated under the flash quenching process [35]. Herein, a facile and superfast Joule heating synthesis method was developed to prepare atomically dispersed Fe-N_4 sites anchored in newly developed defect rich porous carbon spheres support (Fe-N-DCSs) in milliseconds. Density functional theory (DFT) calculations reveal suppressed OH* desorption barrier by armchair-type defect sites, contributing to the excellent ORR kinetics. Resultantly, Fe-N-DCSs is favorable for large half-wave potential ($E_{1/2}$ = 0.90 V) and excellent J_k (34.68 mA cm^{-2}) in O_2-saturated 0.1 M KOH, approaching the highest level among developed ORR electrocatalysts. Moreover, Fe-N-DCSs displays superior long-term ORR durability with only 20 mV attenuation of $E_{1/2}$ after 30000 cycles test. Most importantly, Fe-N-DCSs performs well as an air cathode in the aqueous Zn-air battery (ZAB) with a large maximum power density (224.7 mW cm^{-2}) and long-term cycling stability (1100 h). The as-developed SACs also show prominent performance in the quasi-solid-state Zn-air battery (QSS-ZAB). This work develops novel carbon support with abundant defects and furnishes a practical and feasible method to rationally design efficient SACs with boosting catalytic performance.

2. Experimental section

2.1. Chemicals

Sodium hydroxide (NaOH, ≥ 96.0%) and Potassium hydroxide (KOH, ≥85.0%) were purchased from Sinopharm Chemical Reagent Co., Ltd. Formaldehyde solution (37 wt% in H_2O) and 1,10-Phenanthroline monohydrate (98%) were purchased from Macklin. Pluronic F-127 and Pt/C (20 wt%) were bought from Sigma-Aldrich. Phenol (≥ 99%) and Nafion solution (5 wt%) were bought from Aladdin. Hydrochloric acid (HCl) was purchased from Xilong Scientific. Iron (III) chloride hexahydrate ($FeCl_3\cdot6H_2O$, ≥ 99%) was purchased from J&K Scientific.

2.2. Synthesis of DCS

DCS-precursor was prepared by the hydrothermal method according to the previous report [36]. Subsequently, the obtained precursor was activated by KOH under an Ar atmosphere at 900 ℃ staying 2 h (the weight ratio between DCS-precursor and KOH was four). The DCS was collected after washing with deionized water several times to pH = 7, and drying in the vacuum oven at 60 ℃.

2.3. Synthesis of Fe-N-DCSs

Firstly, 50 mg DCS and 250 mg 1,10-Phenanthroline were mixed uniformly and then were annealed in an N_2 atmosphere at 150 ℃ staying 6 h. The N-DCS was obtained after suction filtration with deionized water, then drying in the vacuum oven at 60 ℃. Secondly, 54 mg $FeCl_3\cdot6H_2O$ and 50 mg N-DCS were added into 20 ml 0.001 M HCl, and the mixed solution was stirring continuously for 2 h. The product Fe, N-DCS, which was absorbed Fe^{3+}, was obtained after suction filtration with deionized water and drying in the vacuum oven.

Finally, the Fe-N-DCSs was obtained by Joule heating at 1200 ℃ in the N_2 atmosphere. The detailed Joule heating process is as follows: The Joule heating equipment manufactured by the company of Shenzhen ZhongKe JingYan (ZKJY-HTS, Fig. S1), was used to synthesize the samples. Firstly, 5 mg of the catalyst was laid on the carbon cloth, which was added to the fixture and linked to direct current power on the sintering table. Next, the reaction system was evacuated and filled with nitrogen. Finally, heating was performed (52 V, 60.5 A) in automatic temperature control mode at 1200 ℃. High-temperature shock enabling transient heating and instantaneous quenching process promotes the synthesis of electrocatalysts.

Fe-N-DCSs-T (T = 1000 ℃; 1200 ℃; 1400 ℃), Fe-N-DCSs-t (t = 1; 2) (T: temperature, t: time) were prepared using the similar procedure of Fe-N-DCSs except for the heating temperature and time. During the synthesis process, the number of Joule heating presents synthesis time.

2.4. Synthesis of N-DCSs

For comparison, the N-DCSs was prepared following similar processes with Fe-N-DCSs without adding $FeCl_3\cdot6H_2O$.

2.5. Characterization

The morphologies of materials were characterized by scanning electron microscope (SEM) on Hitachi Regulus 8100 instrument and transmission electron microcopy (TEM) on a JEM-2100 PLUS. Powder X-ray diffraction (XRD) spectra were tested on a D-MAX 2500/PC diffractometer (Japan Rigaku) operating with Cu radiation. X-ray photoelectron spectroscopy (XPS) was performed on an Axis Supra spectrometer at 15 mA and 14 kV with a monochromatic Al Kα source. Raman spectra were obtained by a Renishaw inVia micro-Raman spectrometer equipped with a 532 nm laser. Nitrogen adsorption-desorption isotherms were determined by a 3Flex Physical Adsorption Analyser (Micrometrics, US). The metal contents were quantified by the inductively coupled plasma atomic emission spectroscopy (Icpoes 730). The aberration-corrected high-angle annular dark-field scanning transmission electron microscopy images were obtained from Titan Cubed Themis G260–300.

2.6. Zn-air batteries measurements

The aqueous Zn-air battery (ZAB) was assembled with 6.0 M KOH and 0.2 M $Zn(Ac)_2$ as the electrolyte, Fe-N-DCSs loaded on carbon paper (1 mg cm^{-2}) as the air cathode, polished Zn flake as the anode. For comparison, we also prepared aqueous ZABs based on Pt/C+RuO_2. The performance of ZABs was evaluated on CHI 760E (Shanghai Chenhua) and Landt battery testing workstations. The design of quasi-solid-state Zn-air battery (QSS-ZAB) was a typical sandwich-like structure, which used polished zinc flake, carbon cloth coated Fe-N-DCSs ink as the anode and air cathode, respectively. The PAM hydrogel prepared according to the previous report was used as the electrolyte [37].

3. Results and discussions

3.1. Catalysts synthesis and physical characterizations

The schematic illustration of Fe-N-DCSs is shown in Fig. 1a. Firstly, defect rich porous carbon spheres (DCS) were prepared by the reported method (Fig. S2a) [36]. DCS maintains the original morphology of nanospheres and shows a porous form. Following that, the N-doped porous carbon spheres (N-DCS, Fig. S2b) were formed using 1,10-Phenanthroline as the nitrogen source. Afterwards, Fe^{3+} was absorbed into N-DCS to form Fe,N-DCS shown in Fig. S3 by impregnation method. In the end, the mixture was subjected to ultrafast thermal shocks by Joule heating in milliseconds and then quenching instantaneously to attain the target material, termed Fe-N-DCSs (Fig. S4). The Fe-N-DCSs was first characterized by scanning electron microscopy (SEM) in Fig. 1b, which has a spherical morphology with about 100 nm in diameter averagly. Transmission electron microscopy (TEM) images further indicate the monodisperse spherical shape of Fe-N-DCSs (Figs. 1c-1d). In addition, SEM and TEM images of N-DCSs in Fig. S5 show that their morphology and structure are identical to Fe-N-DCSs,

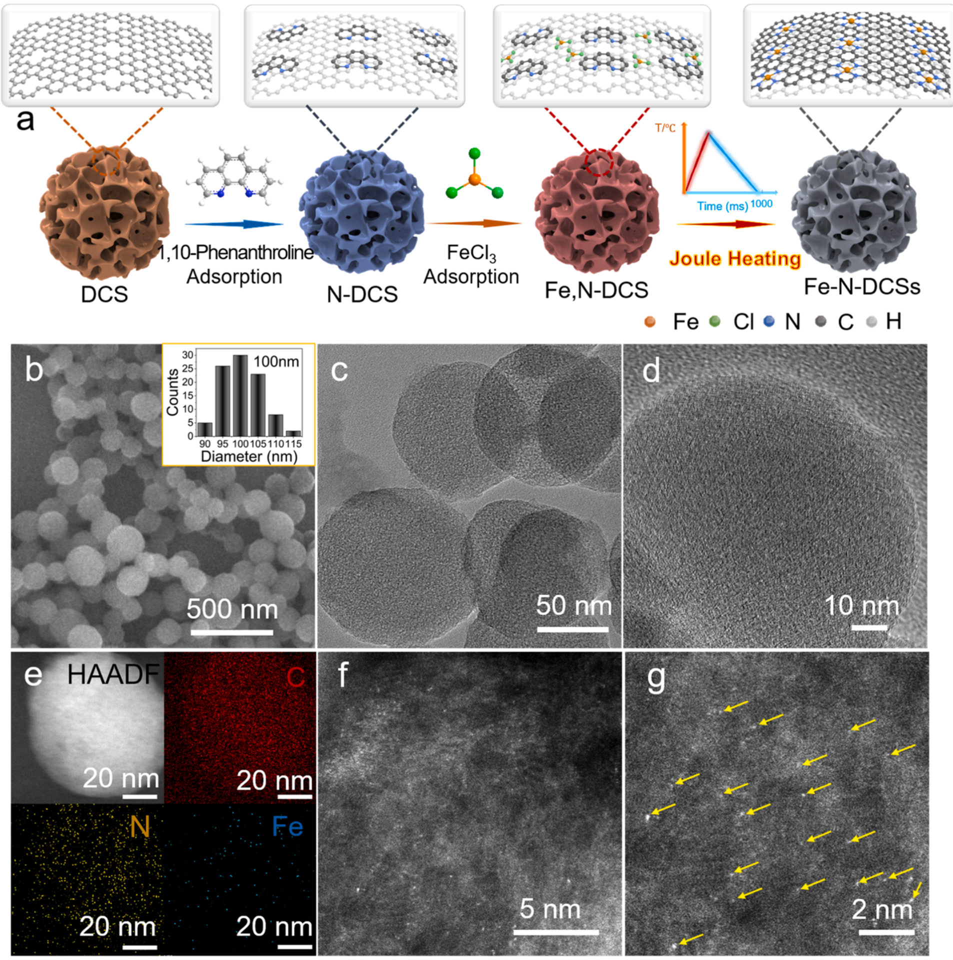

Fig. 1. (a) Schematic illustration of the synthesis for Fe-N-DCSs. (b) SEM image and (c, d) TEM images of Fe-N-DCSs. (e) EDX mapping images of Fe-N-DCSs. (f, g) AC-HAADF-STEM images of Fe-N-DCSs.

which indicates that the morphology of the electrocatalyst would not be affected by the impregnation of Fe atoms.

The porosity structure characteristic of Fe-N-DCSs was investigated by N_2 adsorption-desorption isotherms measurement. The Brauer-Emmet-Teller (BET) surface area of Fe-N-DCSs is up to 1038.5 $m^2\ g^{-1}$ and the pore volume is 0.71 $cm^2\ g^{-1}$ (Fig. S6a, Table S1). In detail, the pore size distributions identified by the Barret-Joyner-Halenda (BJH) and the non-local density functional theory (NLDFT) model, confirm the presence of substantial mesoporous and microporous with the average pore diameter of 2.7 nm (Fig. S6b). Specifically, the micropores in the carbon spheres support could be in favor of accumulating amounts of active sites, while the large surface areas and mesoporous enhance the exposure and accessibility of active sites, thereby increasing ORR activity [38]. The corresponding energy dispersive X-ray (EDX) mapping images in Fig. 1e show that Fe, N, and C are uniformly distributed throughout Fe-N-DCSs. Simultaneously, the aberration-corrected high-angle annular dark-field scanning transmission electron microscopy (AC-HAADF-STEM) images reveal a large number of bright dots representing Fe SAs on Fe-N-DCSs, demonstrating the successful synthesis of SACs (Figs. 1f-1g) [37]. Moreover, the component of Fe in Fe-N-DCSs was detected by inductively coupled plasma-mass spectrometry (ICP-MS) as 0.682 wt%.

The phase structure of Fe-N-DCSs was verified by the X-ray diffraction (XRD) pattern, showing two broad peaks at around 24° and 44°, attributed to the (002) and (101) lattice planes of graphitic carbon, with no other obvious metallic peaks (Fig. 2a) [39]. As shown in Fig. S7, the Raman spectra of Fe-N-DCSs display two characteristic peaks at 1350 and 1580 cm^{-1}, belonging to the D-band to G-band, and the intensity ratio (I_D/I_G) of Fe-N-DCSs (1.05) is comparable to N-DCSs (1.04), indicating that Fe-N-DCSs and N-DCSs are rich in defects [40]. Since the D peak is active in the armchair-type edge and inactive in the zigzag-type edge, it is further concluded that Fe-N-DCSs is abundant in armchair-type defects [41]. Additionally, the surface composition and valence information of Fe-N-DCSs have been studied by X-ray photoelectron spectroscopy (XPS). As depicted in Fig. S8, the XPS survey spectrum reveals the existence of C and N elements in Fe-N-DCSs, while the Fe signal cannot be detected due to the low content. The high-resolution N *1 s* spectrum of Fe-N-DCSs could be deconvoluted into four peaks, which correspond to pyridinic N (398.5 eV), Fe-N_x (399.6 eV), pyrrolic N (400.7 eV) and graphitic N (401.8 eV), respectively (Fig. 2b) [42]. The high-resolution Fe *2p* spectrum is simulated into six peaks in Fig. 2c, which are Fe $2p_{3/2}$ (Fe^{2+} 710.9 eV and Fe^{3+} 714.3 eV), Fe $2p_{1/2}$ (Fe^{2+} 724.8 eV and Fe^{3+} 727.2 eV) and satellite peaks (718.2 eV and 730.2 eV), respectively, indicating the co-existence of Fe^{2+} and Fe^{3+} and predominance of Fe^{2+} in Fe-N-DCSs [43]. Compared with N-DCSs (Fig. S9), the content of pyridinic N in the high-resolution N *1 s* spectrum of Fe-N-DCSs declines noticeably, which might support that pyridinic N is coordinated with Fe to form Fe-N_x (Table S2).

The precise chemical state and coordination environment of Fe atoms in Fe-N-DCSs were determined by X-ray absorption fine structure spectroscopy. As the Fe K-edge XANES spectra of as-developed Fe-N-DCSs and other ferric standards in Fig. 2d show the absorption edge position of Fe-N-DCSs is similar to FePc, indicating around 2^+ oxidation

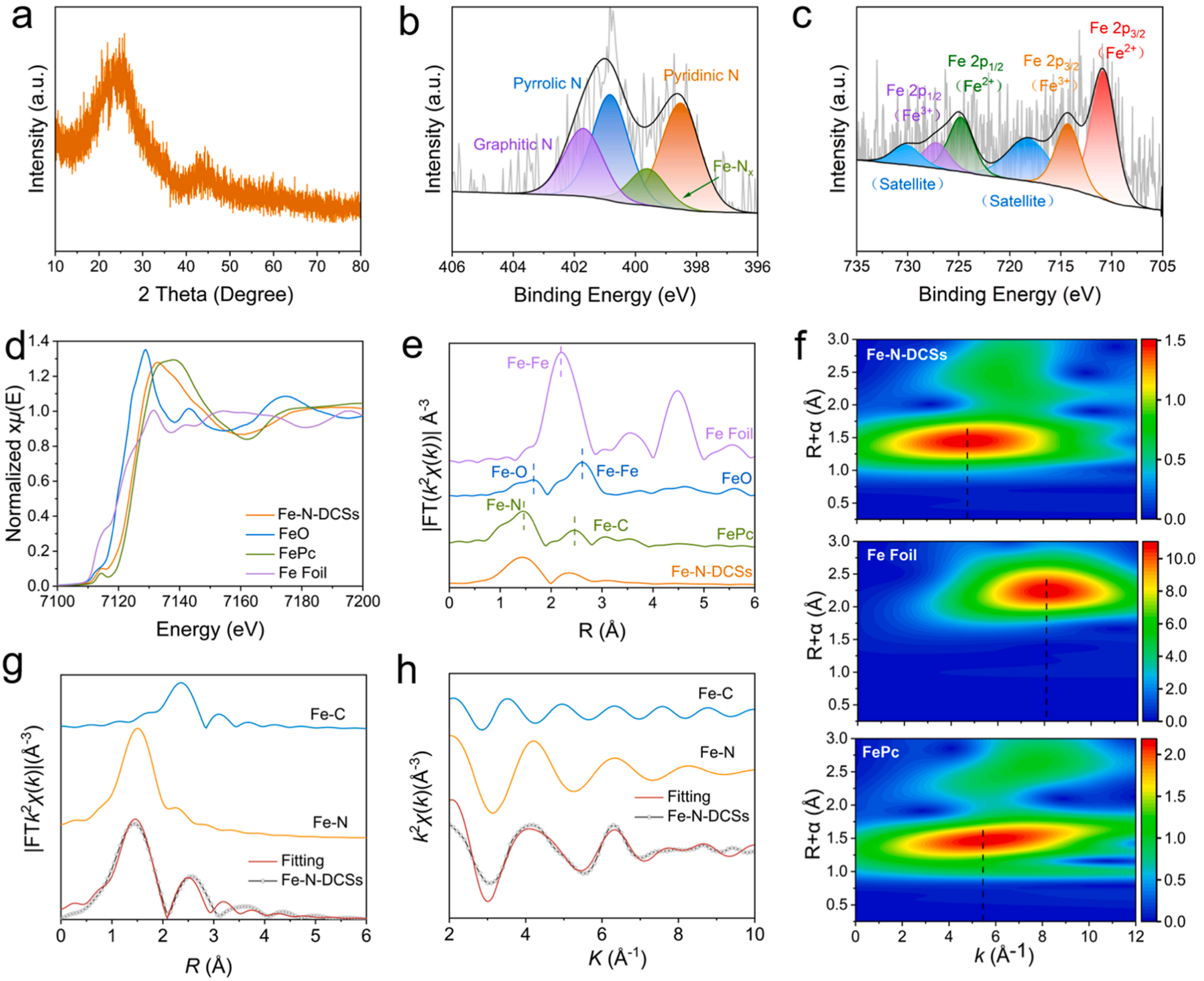

Fig. 2. (a) XRD pattern of Fe-N-DCSs. (b) High-resolution N *1 s* and (c) Fe *2p* spectra of Fe-N-DCSs. (d) Normalized XANES spectra and (e) FT-EXAFS spectra of Fe-N-DCSs, FeO, FePc, and Fe Foil at the Fe K-edge. (f) WT-EXAFS signals of Fe-N-DCSs and relevant reference samples. (g, h) Least squares fittings of FT-EXAFS spectra of Fe-N-DCSs at *R* and *K* space.

state. It is worth noting that the k^2-weight Fourier transformed (FT) EXAFS spectrum for Fe-N-DCSs displays one dominant peak at around 1.5 Å and another at around 2.5 Å, corresponding to the first coordination shell of the Fe-N and second coordination shell of Fe-C co-ordinations (Fig. 2e) [44]. Additionally, by comparing with the FT-EXAFS spectra of Fe Foil and FeO, Fe-N-DCSs shows no characteristic peaks of Fe-Fe bond, confirming that Fe atoms are atomically dispersed, which shows no differences with the results of mapping and AC-HAADF-STEM mentioned above [45]. To further confirm more information about coordination configurations of Fe in Fe-N-DCSs, wavelet transform (WT) EXAFS analysis was performed. As shown in Fig. 2f and Fig. S10, only one maximum contour intensity position located at 1.5 Å in the R space of Fe-N-DCSs is detected, which is assigned to the Fe-N bond [46]. The above analysis is almost identical to that of FePc, certificating the Fe dispersed atomically in Fe-N-DCSs without the formation of Fe clusters or nanoparticles and the successful synthesis of target SACs. Following that, the exact coordination configuration and structure parameters of Fe-N-DCSs were analyzed by least squares fittings of FT-EXAFS spectra in R and K-space (Figs. 2g-2h). The fitting results shown in Table S3 deliver that the first coordination configurations shell of Fe atoms in Fe-N-DCSs is Fe-N with a bond length of 2.03 Å and the coordination number is about 5.13, indicating the successful formation of Fe-N_4 sites with an axial O atom absorbed from the adsorbed oxygen on the carbon support, and the presence of axial oxygen atom bound to Fe has no influence on the planarity of FeN_4 [47, 48]. Meanwhile, the second coordination shell is Fe-C, which has a bond length of 2.99 Å and a coordination number of about 4.45.

3.2. Electrocatalytic properties measurement

The electrocatalytic ORR activities of Fe-N-DCSs and Pt/C were evaluated via the rotating disk electrode (RDE) in O_2-saturated 0.1 M KOH solution. The Fe-free defect rich porous carbon spheres (N-DCSs) were also prepared by the same procedure without adding Fe^{3+} as a comparison (Fig. S5). To deeply explore the relationship between synthetic conditions and the catalytic performance of electrocatalysts, ORR polarization curves were compared (Fig. S11). These results indicate that suitable synthetic conditions can remarkably boost the ORR activity. Cyclic voltammetry (CV) plots show that the as-developed Fe-N-DCSs has the highest oxygen reduction peak (0.84 V), indicating the remarkable electrochemical activity towards the ORR (Fig. S12). As shown in Fig. 3a, Fe-N-DCSs exhibits a higher onset potential (E_{onset} =

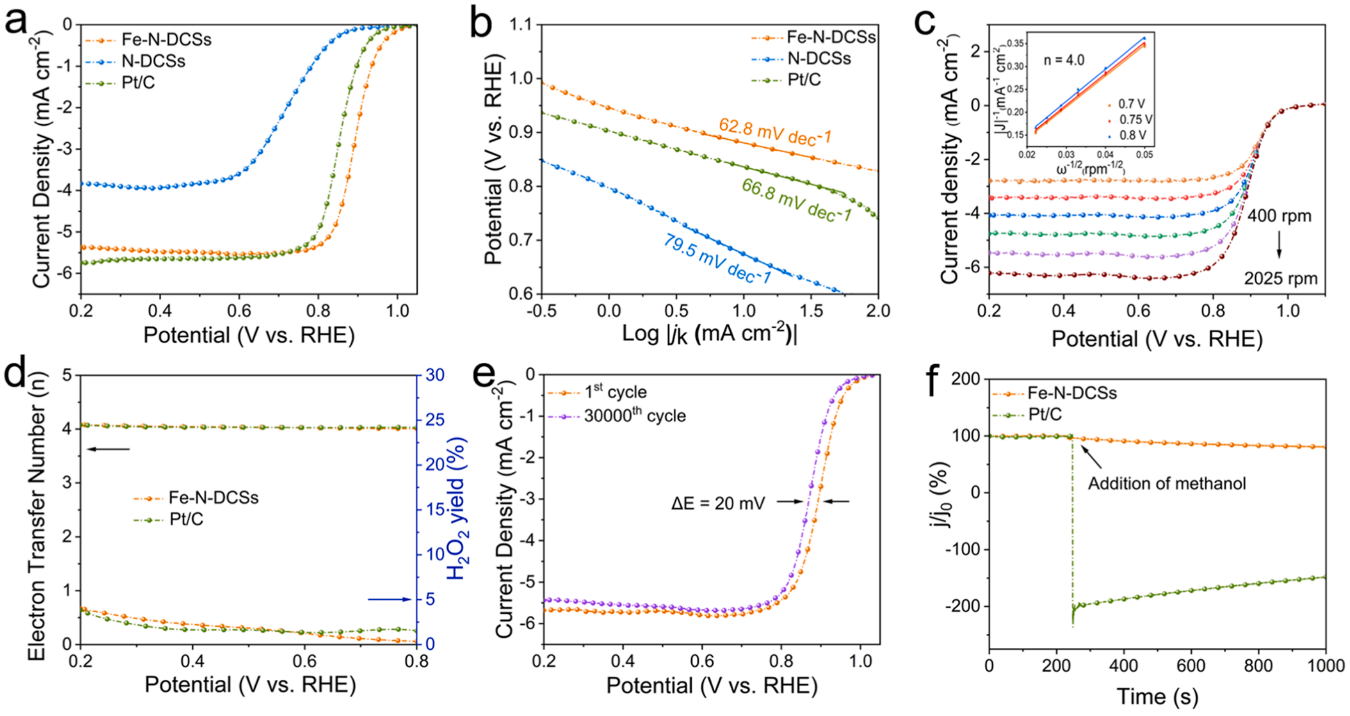

Fig. 3. (a) ORR linear sweep voltammetry (LSV) curves (b) the corresponding Tafel plots of Fe-N-DCSs, N-DCSs, and Pt/C obtained in O_2-saturated 0.1 M KOH at 1600 rpm. (c) ORR LSV curves of Fe-N-DCSs recorded at different rotating speeds. (The inset is the corresponding K-L plots). (d) H_2O_2 yield and n of Fe-N-DCSs and Pt/C. (e) 1st and 30000th LSV polarization curves of Fe-N-DCSs in O_2-saturated 0.1 M KOH. (f) Comparison of methanol tolerances of Fe-N-DCSs and Pt/C with the addition of methanol.

1.00 V) and half-wave potential ($E_{1/2}$ = 0.90 V) than Pt/C (E_{onset} = 0.95 V, $E_{1/2}$ = 0.85 V), N-DCSs (E_{onset} = 0.87 V, $E_{1/2}$ = 0.73 V) and catalysts reported recently (Table S6). Furthermore, the Tafel slopes in Fig. 3b reflect that the kinetics of Fe-N-DCSs (62.8 mV dec^{-1}) is comparable to that of Pt/C (66.8 mV dec^{-1}), and less that of N-DCSs (79.5 mV dec^{-1}), an additional proof of its outstanding ORR kinetics [49]. Fe-N-DCSs has a record kinetic current density (J_k) value of 34.68 mA cm^{-2} at 0.85 V, exceeding N-DCSs and Pt/C by 115- and 5.8-fold, since the high J_k also means excellent ORR activity (Fig. S13) [50]. The double-layer capacitance (C_{dl}) was utilized to evaluate the electrochemical surface area (ECSA). As presented in Fig. S14, Fe-N-DCSs has the highest calculated C_{dl} value of 9.05 mF cm^{-2} than N-DCSs (4.22 mF cm^{-2}) and Pt/C (4.76 mF cm^{-2}), indicating the large surface area of Fe-N-DCSs, which allows full exposure of the active sites [51]. Besides, based on Koutecky-Levich's (K-L) equation, the efficient four-electron transfer pathway is extrapolated by the LSV curves of Fe-N-DCSs at different rotational speeds (400 rpm to 2025 rpm, Fig. 3c). Additionally, the rotating ring electrode (RRDE) test in Fig. 3d and Fig. S15 confirms the electron transfer number (n) is about 4, following the results calculated of the K-L equation calculations, accompanied by a lower hydrogen peroxide (H_2O_2) yield (below 4%) with the potential in the range of 0.2–0.8 V, suggesting its superior selectivity of Fe-N-DCSs toward four-electron mediated ORR processes.

Apart from the electrocatalytic activity, the stability of catalysts also plays an indispensable role in practical applications, which was assessed by accelerated degradation test (ADT) and chronoamperometric i-t curves. As demonstrated by the ADT, Fe-N-DCSs lost only 20 mV of $E_{1/2}$ after 30,000 cycles (Fig. 3e). In addition, as shown in Fig. S16, the current density retention rate of Fe-N-DCSs is 95.1% after operating for 50 h continuously, which is significantly better than Pt/C (81.3%). All these indicate that Fe-N-DCSs has excellent durability. Impressively, the morphology of Fe-N-DCSs in Fig. S17 remains unchanged after the ADT testing. EDX mapping images in Fig. S18 verify the homogeneous distribution of all elements (C, N and Fe) throughout Fe-N-DCSs after the chronoamperometric i-t test. AC-HAADF-STEM images reveal that Fe in Fe-N-DCSs still remains as SAs and no agglomeration occurs after ADT testing (Fig. S19). It also can be seen from XPS in Fig. S20 that the valence states of N and Fe in the catalyst have no significant change, and from the ICP, the Fe loading has a marginal lost of only 0.007 wt%. All these further confirm the outstanding stability of Fe-N-DCSs. Moreover, negligible ORR current density of Fe-N-DCSs can be found after adding methanol into the electrolyte, inferring a favorable methanol tolerance of Fe-N-DCSs in an alkaline environment (Fig. 3f). All these results corroborate the excellent ORR activities of Fe-N-DCSs, which has exceptional potential for practical applications.

3.3. DFT calculations

To elucidate the origin of the excellent ORR performance achieved by Fe-N-DCSs, DFT calculation using the Vienna ab initio Simulation Package (VASP) was carried out. Our previous studies have shown that the substitution of the nearest carbon atom at the Fe-(N-C_2)$_4$ site with N is one of the stabilized conformations and the defects take a more critical role in accelerating ORR kinetics [52]. Therefore, we constructed four typical configurations including armchair-type edge and zigzag-type edge defects of Fe-(N-C_2)$_4$ and N-doped Fe-(N-C_2)$_4$-N, named A-Fe-(N-C_2)$_4$, A-Fe-(N-C_2)$_4$-N, Z-Fe-(N-C_2)$_4$ and Z-Fe-(N-C_2)$_4$-N respectively, to investigate the effects of different edge-type defects around the active site of Fe-N_4 on the ORR performance (Fig. S21). The adsorption configurations of the DFT-optimized ORR intermediates on different models were then systematically explored in Fig. 4a and Fig. S22-S24. Accordingly, the changes in the free energy about the four-electron transfer pathway for different models at U = 0 V and U = 1.23 V were calculated. Under the equilibrium potential (U) = 0 V (Fig. 4b and Table S4), the calculated adsorption-free energies of the intermediates tend to decrease for the four configurations, suggesting exothermic and spontaneous ORR processes. Specifically, it has been exhaustively confirmed that the OH* desorption step is considered the

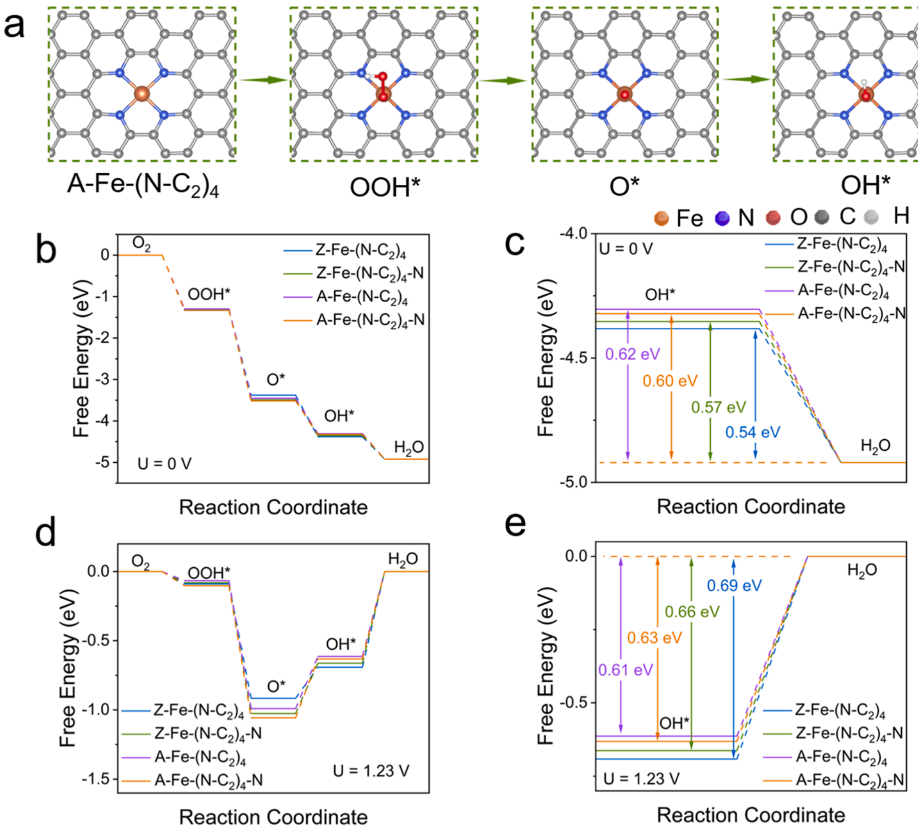

Fig. 4. (a) DFT-optimized adsorption configurations of ORR intermediates on A-Fe-(N-C_2)$_4$. (b,c) Free energy diagram of the four-electron ORR process and the OH* desorption step on A-Fe-(N-C_2)$_4$, A-Fe-(N-C_2)$_4$-N, Z-Fe-(N-C_2)$_4$ and Z-Fe-(N-C_2)$_4$-N at U = 0 V. (d,e) Free energy diagram of the four-electron ORR process and the OH* desorption step on A-Fe-(N-C_2)$_4$, A-Fe-(N-C_2)$_4$-N, Z-Fe-(N-C_2)$_4$ and Z-Fe-(N-C_2)$_4$-N at U = 1.23 V.

rate-determining step (RDS) for Fe-N_4 active sites. In particular, as depicted in Fig. 4c, the ΔG_{OH^*} (0.62 eV) for A-Fe-(N-C_2)$_4$ configuration is similar to that of A-Fe-(N-C_2)$_4$-N (0.60 eV), but significantly higher than ΔG_{OH^*} for Z-Fe-(N-C_2)$_4$-N (0.57 eV) and Z-Fe-(N-C_2)$_4$ (0.54 eV), which suggests that A-Fe-(N-C_2)$_4$ with armchair-type edge defects have the largest OH* adsorption free energy, benefiting to the OH* desorption step and boosting the ORR performance [53]. This proves that armchair-type edge defects can promote the adsorption-desorption behaviors of ORR intermediates. At U = 1.23 V (Fig. 4d-4e and Table S5), the whole reaction consists of exothermic and absorptive steps, where the differences in free energy, especially the endothermic step, were discussed. The endothermic step with the largest free energy difference, the desorption process of OH*, is the RDS for all configurations [54]. Particularly, A-Fe-(N-C_2)$_4$ shows an overpotential of 0.61 V, lower than the overpotential of Z-Fe-(N-C_2)$_4$ (0.69 V). Simultaneously, the overpotential of Z-Fe-(N-C_2)$_4$-N (0.66 eV) is inferior to Z-Fe-(N-C_2)$_4$ (0.69 eV). Consequently, the armchair-type edge defects decorated Fe-N_4 active site possess a lower energy barrier for OH* desorption than the zigzag-type edge defects, resulting in the improvement of intrinsic ORR activity. In brief, armchair-type defects do have important implications for ORR.

3.4. Zn-air battery performance

During the charging process of Zn-air batteries (ZABs), the air electrode experiences an oxygen evolution reaction (OER) [55]. Therefore, the OER performance of Fe-N-DCSs was evaluated in 1 M KOH by RDE. In Fig. S25a, the OER polarization curves demonstrate that Fe-N-DCSs achieves the current density of 10 mA cm^{-2} at a potential of 1.57 V, similar to the reference RuO_2 (1.53 V). Meanwhile, the Tafel slope of Fe-N-DCSs (66.3 mV dec^{-1}) is in proximity to that of RuO_2 (62.3 mV dec^{-1}, Fig. S25b), indicating that Fe-N-DCSs has sound OER activity and kinetics.

Given the outstanding bi-functional activity of Fe-N-DCSs, we further evaluated the application potential of Fe-N-DCSs in ZABs, compared with ZAB based on Pt/C + RuO_2. As shown in Fig. 5a, the aqueous ZAB is assembled using Fe-N-DCSs as the air cathode and polished Zn flake as the anode, 6 M KOH + 0.2 M Zn(Ac)$_2$ as the electrolyte. The open circuit plots (OCP) of aqueous ZABs based on Fe-N-DCSs in Fig. S26 remain at 1.48 V, higher than that of Pt/C + RuO_2 (1.37 V). Fe-N-DCSs-based ZAB achieves a higher peak power density of 224.7 mW cm^{-2} than Pt/C + RuO_2 (172.5 mW cm^{-2}, Fig. 5b). Moreover, ZAB based on Fe-N-DCSs shows a specific capacity of 790 mA h g^{-1} at 10 mA cm^{-2} (Fig. S27), outperforming ZAB based on Pt/C + RuO_2 (748 mA h g^{-1}). All these demonstrate that the assembled aqueous ZAB has exceptional performance. Furthermore, the variations in voltages of Fe-N-DCSs and Pt/C + RuO_2-based ZAB were examined at different current densities. Fig. 5c shows that the discharge curve voltages of Fe-N-DCSs and Pt/C + RuO_2-based ZAB decrease as the current density increases to 50 mA cm^{-2}, however, the voltage returns to the initial state as the current density gradually decreases. Impressively, Fe-N-DCSs-based ZAB possesses a constantly higher voltage than that of Pt/C + RuO_2 under the same current density (1–50 mA cm^{-2}), in particular, even at a high current density of 50 mA cm^{-2}, the Fe-N-DCSs maintains at 1.15 V, while the Pt/C + RuO_2 is only 1.0 V, signifying the excellent rate capability of Fe-N-DCSs.

Using galvanostatic discharge/charge measurement to further assess the cycling stability of the battery. The ZAB constructed by Fe-N-DCSs has remarkable stability, with an initial charge-discharge voltage gap around 0.92 V, keeping constant even after 1100 h continuous charge-discharge cycles at 10 mA cm^{-2} with voltage gap still around 0.92 V, while the gap of aqueous ZAB based on the Pt/C + RuO_2 catalyst rises

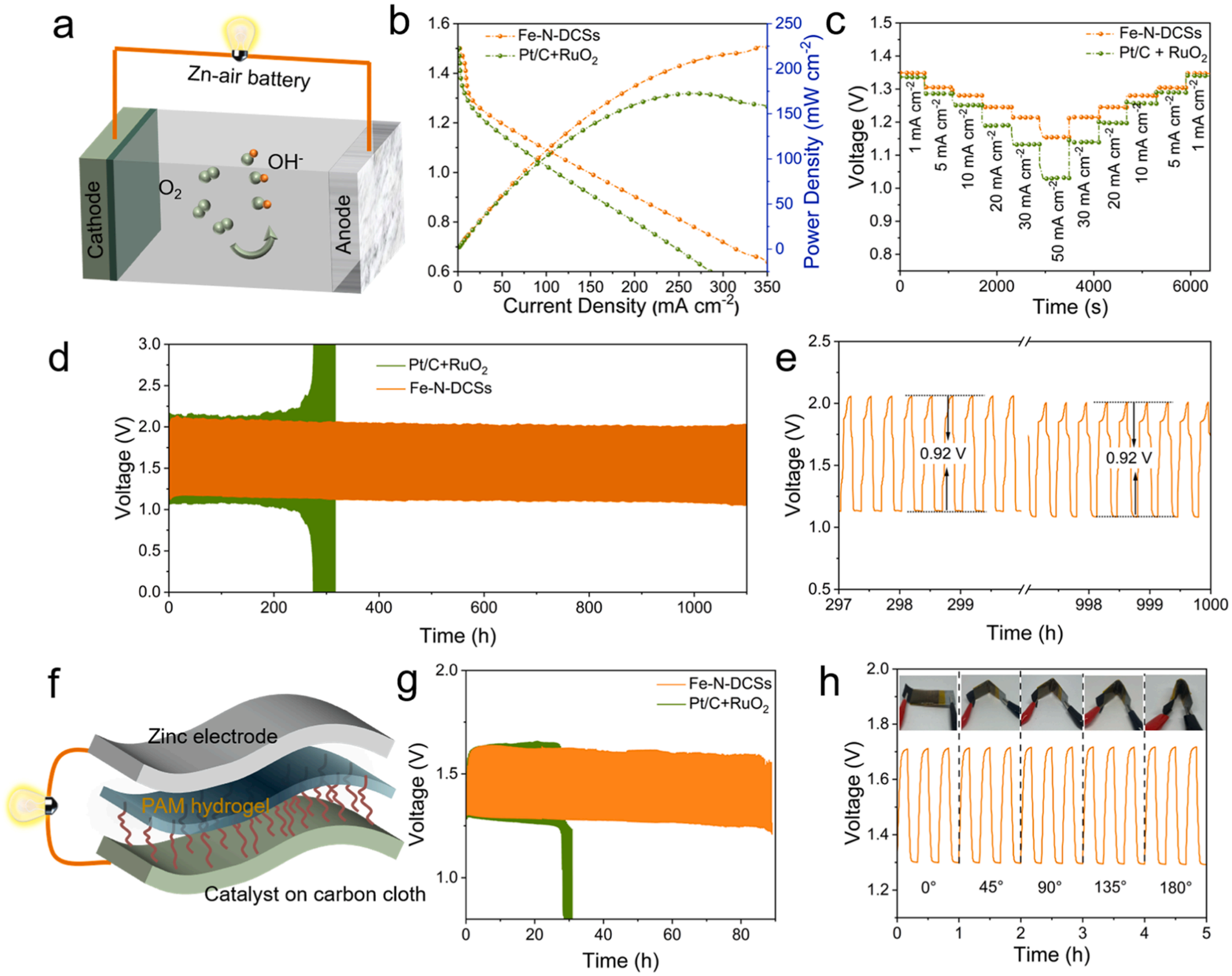

Fig. 5. (a) Schematic illustration of the aqueous ZAB. (b) Power density and discharge curves of aqueous ZABs assembled by Fe-N-DCSs and Pt/C + RuO_2. (c) Rate performance of aqueous ZABs assembled by Fe-N-DCSs and Pt/C + RuO_2 at different current densities from 1 to 50 mA cm^{-2}. (d) Discharge/charge cycling performance of aqueous ZABs based on Fe-N-DCSs and Pt/C + RuO_2 at a current density of 10 mA cm^{-2}. (e) Discharge/charge voltage gap of aqueous ZABs based on Fe-N-DCSs during the cycling test. (f) Schematic illustration of the QSS-ZAB. (g) Discharge/charge cycling performance of QSS-ZABs based on Fe-N-DCSs and Pt/C + RuO_2 at a current density of 1 mA cm^{-2}. (h) Discharge/charge curves of QSS-ZABs based on Fe-N-DCSs under different bending angles.

dramatically after 200 h with voltage gap of 1.08 V (Figs. 5d and 5**e**). Impressively, the voltage efficiency of Fe-N-DCSs-based ZAB decreases from 54.8% to 53.8% during charging and discharging from 200 to 1000 h in Fig. S28, a decrease of only 1% further indicating the excellent durability of Fe-N-DCSs-based ZAB [56]. Overall, by comparing with the recent reports, the electrochemical performance of aqueous ZAB driven by Fe-N-DCSs is more outstanding than most reported ZAB (Table S7). All these results indicate that as-developed Fe-N-DCSs exhibits a high potential to be an exceptional candidate for ZAB air cathode.

Quasi-solid-state Zn-air battery (QSS-ZAB), the most attractive energy technology for wearable electrons has received widespread attention [57]. Meanwhile, to broaden the usefulness of Fe-N-DCSs, we prepared QSS-ZAB using Fe-N-DCSs loaded on carbon cloth as air cathode, polished zinc flakes as the anode, and PVA hydrogel as the electrolyte, compared with QSS-ZAB based on Pt/C + RuO_2 (Fig. 5f) [37]. As shown in Fig. S29, the QSS-ZAB based on the Fe-N-DCSs shows an OCP of 1.46 V and a specific capacity of 746 mA h g^{-1}, outperforming QSS-ZAB based on Pt/C+RuO_2 (1.36 V and 698 mA h g^{-1}). In addition, the QSS-ZAB based on Fe-N-DCSs possesses a better current density at the same voltage and the power density (266.3 mW cm^{-2}) is 1.3-fold higher than Pt/C+RuO_2 (Fig. S30), revealing the outstanding performance of assembled QSS-ZAB. Simultaneously, when testing from 0.5 mA cm^{-2} to 10 mA cm^{-2} and then back to 0.5 mA cm^{-2} in Fig. S31, the discharge potentials of QSS-ZAB based on Fe-N-DCSs and Pt/C+RuO_2 return to the initial state. Surprisedly, the QSS-ZAB based on Fe-N-DCSs delivers a higher current density of 1.21 V than Pt/C + RuO_2 of 1.19 V even at 10 mA cm^{-2}, which demonstrates the attractive rate capability of Fe-N-DCSs-based QSS-ZAB. Most crucially, the QSS-ZAB based on Fe-N-DCSs remains a consistent voltage gap of 0.34 V throughout the charge-discharge processes for nearly 90 h, while Pt/C + RuO_2-based QSS-ZAB only remains a stable continuous for 25 h with voltage gap of 0.40 V (Fig. 5g and Fig. S32). Fig. 5h illustrates that the Fe-N-DCSs-based QSS-ZAB can cycle stably even bending to different angles, proving its impressive stability and flexibility. These results show the promise of our fabricated Fe-N-DCSs-based quasi-solid-state and aqueous ZABs for practical applications.

4. Conclusion

In summary, this work introduces a novel method for the controlled synthesis of SACs with atomically dispersed Fe-N_4 active sites on newly developed porous carbon spheres support through super-fast Joule heating in milliseconds. The fabricated Fe-N-DCSs possesses rich defects, which accommodates and fully exposes a wide range of SA active sites. We demonstrate that the armchair-type defects decorated Fe-N_4 active sites have a lower energy barrier for OH* desorption. This offers critical insights into the key role of armchair-type defects during the ORR process. Thereby, Fe-N-DCSs affords a superior high ORR activity of $E_{1/2}$ and J_k up to 0.90 V and 34.68 mA cm^{-2} in 0.1 M KOH, respectively. Furthermore, Fe-N-DCSs also delivers excellent working durability for virtually nearly no lost of $E_{1/2}$ after 30,000 cycles. Impressively, the aqueous ZAB assembled with Fe-N-DCSs affords excellent long-term galvanostatic charge-discharge cycling durability for 1100 h and also performs well in QSS-ZAB. This work presents a large step forward in the design and ultrafast fabrication of SACs with high catalytic performance.

CRediT authorship contribution statement

Yifei Liu: Investigation, Data curation, Conceptualization, Formal analysis, Validation, Writing – original draft. **Lingbo Zong**: Conceptualization, Writing-review, Supervision, Funding acquisition. **Yuanyuan Zhang**: Data curation, Validation. **Fenghong Lu**: Investigation, Data curation. **Lei Wang**: Funding acquisition, Supervision.

Declaration of Competing Interest

The authors declare that they have no known competing financial interests or personal relationships that could have appeared to influence the work reported in this paper.

Data availability

Data will be made available on request.

Acknowledgement

This work was supported financially by the National Natural Science Foundation of China, China (Grant No. 52172208, 52072197, 52272222), Taishan Scholar Young Talent Program (tsqn201909114, tsqn202306216), XAS beamlines at the Australian Synchrotron in Melbourne are gratefully acknowledged.

Appendix A. Supporting information

Supplementary data associated with this article can be found in the online version at doi:10.1016/j.apcatb.2024.124673.

References

[1] P. Guo, B. Liu, F. Tu, Y. Dai, Z. Zhang, Y. Xia, M. Ma, Y. Zhang, L. Zhao, Z. Wang, Breaking sabatier's vertex via switching the oxygen adsorption configuration and reaction pathway on dual active sites for acidic oxygen reduction, Energy Environ. Sci. 17 (2024) 3077–3087, https://doi.org/10.1039/d4ee00823e.

[2] R.Z. Snitkoff-Sol, O. Rimon, A.M. Bond, L. Elbaz, Direct measurement of the oxygen reduction reaction kinetics on iron phthalocyanine using advanced transient voltammetry, Nat. Catal. 7 (2024) 139–147, https://doi.org/10.1038/s41929-023-01086-0.

[3] L. Zhang, T. Gu, K. Lu, L. Zhou, D.S. Li, R. Wang, Engineering synergistic edge-N dipole in metal-free carbon nanoflakes toward intensified oxygen reduction electrocatalysis, Adv. Funct. Mater. 31 (2021) 2103187, https://doi.org/10.1002/adfm.202103187.

[4] M. Liu, J. Zhang, H. Su, Y. Jiang, W. Zhou, C. Yang, S. Bo, J. Pan, Q. Liu, In situ modulating coordination fields of single-atom cobalt catalyst for enhanced oxygen reduction reaction, Nat. Commun. 15 (2024) 1675, https://doi.org/10.1038/s41467-024-45990-w.

[5] J. Li, T. Lu, Y. Fang, G. Zhou, M. Zhang, H. Pang, J. Yang, Y. Tang, L. Xu, The manipulation of rectifying contact of Co and nitrogen-doped carbon hierarchical superstructures toward high-performance oxygen reduction reaction, Carbon Energy (2024) e529, https://doi.org/10.1002/cey2.529.

[6] Y. Zhou, R. Lu, X. Tao, Z. Qiu, G. Chen, J. Yang, Y. Zhao, X. Feng, K. Müllen, Boosting oxygen electrocatalytic activity of Fe-N-C catalysts by phosphorus incorporation, J. Am. Chem. Soc. 145 (2023) 3647–3655, https://doi.org/10.1021/jacs.2c12933.

[7] L. Gloag, S.V. Somerville, J.J. Gooding, R.D. Tilley, Co-catalytic metal-support interactions in single-atom electrocatalysts, Nat. Rev. Mater. 9 (2024) 173–189, https://doi.org/10.1038/s41578-023-00633-2.

[8] Y. Li, S. Yin, L. Chen, X. Cheng, C. Wang, Y. Jiang, S. Sun, Boost the utilization of dense FeN$_4$ sites for high-performance proton exchange membrane fuel cells, Energy Environ. Mater. 7 (2023) e12611, https://doi.org/10.1002/eem2.12611.

[9] H. Xia, R. Pang, X. Dong, Q. Liu, J. Chen, E. Wang, J. Li, Boosting oxygen reduction reaction kinetics by designing rich vacancy coupling pentagons in the defective carbon, J. Am. Chem. Soc. 145 (2023) 25695–25704, https://doi.org/10.1021/jacs.3c08556.

[10] Y. Shin, Y. Lee, C. Jo, Y.H. Kim, S. Park, Co(O)$_4$(N)-type single-atom-based catalysts and ligand-driven modulation of electrocatalytic properties for reducing oxygen molecules, EcoEnergy 2 (2024) 154–168, https://doi.org/10.1002/ece2.27.

[11] X. Qiu, Y. Wang, M. Shao, High-performance and durable Fe-N-C fuel cell catalysts, Joule 8 (2024) 881–882, https://doi.org/10.1016/j.joule.2024.03.018.

[12] L. Zong, K. Fan, W. Wu, L. Cui, L. Zhang, B. Johannessen, D. Qi, H. Yin, Y. Wang, P. Liu, L. Wang, H. Zhao, Anchoring single copper atoms to microporous carbon spheres as high-performance electrocatalyst for oxygen reduction reaction, Adv. Funct. Mater. 31 (2021) 2104864, https://doi.org/10.1002/adfm.202104864.

[13] Y. Chen, Z. Li, Y. Zhu, D. Sun, X. Liu, L. Xu, Y. Tang, Atomic Fe dispersed on N-doped carbon hollow nanospheres for high-efficiency electrocatalytic oxygen reduction, Adv. Mater. 31 (2018) 1806312, https://doi.org/10.1002/adma.201806312.

[14] N. Li, M. Li, K. Guo, Z. Guo, R. Wang, L. Bao, G.L. Hou, X. Lu, Deciphering the role of native defects in dopant-mediated defect engineering of carbon electrocatalysts, Adv. Energy Mater. (2024) 2401008, https://doi.org/10.1002/aenm.202401008.

[15] S. Liu, C. Li, M.J. Zachman, Y. Zeng, H. Yu, B. Li, M. Wang, J. Braaten, J. Liu, H. M. Meyer, M. Lucero, A.J. Kropf, E.E. Alp, Q. Gong, Q. Shi, Z. Feng, H. Xu, G. Wang, D.J. Myers, J. Xie, D.A. Cullen, S. Litster, G. Wu, Atomically dispersed iron sites with a nitrogen-carbon coating as highly active and durable oxygen reduction catalysts for fuel cells, Nat. Energy 7 (2022) 652–663, https://doi.org/10.1038/s41560-022-01062-1.

[16] W. Xu, R. Zeng, M. Rebarchik, A. Posada-Borbón, H. Li, C.J. Pollock, M. Mavrikakis, H.D. Abruña, Atomically dispersed Zn/Co-N-C as ORR electrocatalysts for alkaline fuel cells, J. Am. Chem. Soc. 146 (2024) 2593–2603, https://doi.org/10.1021/jacs.3c11355.

[17] Z. Guo, S. Yang, M. Liu, Q. Xu, G. Zeng, Construction of imide-linked covalent organic frameworks with palladium nanoparticles for oxygen reduction reaction, EcoEnergy 2 (2024) 192–201, https://doi.org/10.1002/ece2.32.

[18] Y. Yao, Z. Huang, P. Xie, L. Wu, L. Ma, T. Li, Z. Pang, M. Jiao, Z. Liang, J. Gao, Y. He, D.J. Kline, M.R. Zachariah, C. Wang, J. Lu, T. Wu, T. Li, C. Wang, R. Shahbazian-Yassar, L. Hu, High temperature shockwave stabilized single atoms, Nat. Nanotechnol. 14 (2019) 851–857, https://doi.org/10.1038/s41565-019-0518-7.

[19] B. Deng, Z. Wang, W. Chen, J.T. Li, D.X. Luong, R.A. Carter, G. Gao, B.I. Yakobson, Y. Zhao, J.M. Tour, Phase controlled synthesis of transition metal carbide nanocrystals by ultrafast flash joule heating, Nat. Commun. 13 (2022) 262, https://doi.org/10.1038/s41467-021-27878-1.

[20] S. Ji, Y. Chen, X. Wang, Z. Zhang, D. Wang, Y. Li, Chemical synthesis of single atomic site catalysts, Chem. Rev. 120 (2020) 11900–11955, https://doi.org/10.1021/acs.chemrev.9b00818.

[21] K.M. Wyss, D.X. Luong, J.M. Tour, Large-scale syntheses of 2d materials: flash joule heating and other methods, Adv. Mater. 34 (2022) 2106970, https://doi.org/10.1002/adma.202106970.

[22] S. Wei, A. Li, J.-C. Liu, Z. Li, W. Chen, Y. Gong, Q. Zhang, W.-C. Cheong, Y. Wang, L. Zheng, H. Xiao, C. Chen, D. Wang, Q. Peng, L. Gu, X. Han, J. Li, Y. Li, Direct observation of noble metal nanoparticles transforming to thermally stable single atoms, Nat. Nanotechnol. 13 (2018) 856–861, https://doi.org/10.1038/s41565-018-0197-9.

[23] X. Yan, D. Liu, P. Guo, Y. He, X. Wang, Z. Li, H. Pan, D. Sun, F. Fang, R. Wu, Atomically dispersed Co$_2$MnN$_8$ triatomic sites anchored in n-doped carbon enabling efficient oxygen reduction reaction, Adv. Mater. 35 (2023) 2210975, https://doi.org/10.1002/adma.202210975.

[24] L. Zong, K. Fan, L. Cui, F. Lu, P. Liu, B. Li, S. Feng, L. Wang, Constructing Fe-N$_4$ sites through anion exchange-mediated transformation of Fe coordination environments in hierarchical carbon support for efficient oxygen reduction, Angew. Chem. Int. Ed. 62 (2023) e202309784, https://doi.org/10.1002/anie.202309784.

[25] H. Fei, J. Dong, C. Wan, Z. Zhao, X. Xu, Z. Lin, Y. Wang, H. Liu, K. Zang, J. Luo, S. Zhao, W. Hu, W. Yan, I. Shakir, Y. Huang, X. Duan, Microwave-assisted rapid synthesis of graphene-supported single atomic metals, Adv. Mater. 30 (2018) 1802146, https://doi.org/10.1002/adma.201802146.

[26] Y. Huang, J. Xiong, Z. Zou, Z. Chen, Emerging strategies for the synthesis of correlated single atom catalysts, Adv. Mater. (2024) 2312182, https://doi.org/10.1002/adma.202312182.

[27] W. Yan, X. Wang, M. Liu, K. Ma, L. Wang, Q. Liu, C. Wang, X. Jiang, H. Li, Y. Tang, G. Fu, PCTS-controlled synthesis of L1$_0$/L1$_2$-typed Pt-Mn intermetallics for electrocatalytic oxygen reduction, Adv. Funct. Mater. 34 (2023) 2310487, https://doi.org/10.1002/adfm.202310487.

[28] D. Xi, J. Li, J. Low, K. Mao, R. Long, J. Li, Z. Dai, T. Shao, Y. Zhong, Y. Li, Z. Li, X. J. Loh, L. Song, E. Ye, Y. Xiong, Limiting the uncoordinated n species in M-N$_x$ single-atom catalysts toward electrocatalytic CO$_2$ reduction in broad voltage range, Adv. Mater. 34 (2021) 2104090, https://doi.org/10.1002/adma.202104090.

[29] Y. Qiu, Z. Hu, H. Li, Q. Ren, Y. Chen, S. Hu, Hybrid electrocatalyst Ag/Co/C via flash joule heating for oxygen reduction reaction in alkaline media, Chem. Eng. J. 430 (2022) 132769, https://doi.org/10.1016/j.cej.2021.132769.

[30] D. Xia, J. Mannering, P. Huang, Y. Xu, Q. Li, H. Li, Y. Qin, A.N. Kulak, R. Menzel, Electrothermal transformations within graphene-based aerogels through high-temperature flash joule heating, J. Am. Chem. Soc. 146 (2023) 159–169, https://doi.org/10.1021/jacs.3c06349.

[31] G. He, M. Yan, H. Gong, H. Fei, S. Wang, Ultrafast synthetic strategies under extreme heating conditions toward single-atom catalysts, Int. J. Extrem. Manuf. 4 (2022) 032003, https://doi.org/10.1088/2631-7990/ac670b.

[32] Y. Dong, Y. Rao, H. Liu, H. Zhang, R. Hu, Y. Chen, Y. Yao, H. Yang, Highly efficient chemical production via electrified, transient high-temperature synthesis, eScience 4 (2024) 100253, https://doi.org/10.1016/j.esci.2024.100253.

[33] K. Zeng, J. Zhang, W. Gao, L. Wu, H. Liu, J. Gao, Z. Li, J. Zhou, T. Li, Z. Liang, B. Xu, Y. Yao, Surface-decorated high-entropy alloy catalysts with significantly boosted activity and stability, Adv. Funct. Mater. 32 (2022) 2204643, https://doi.org/10.1002/adfm.202204643.

[34] D.X. Luong, K.V. Bets, W.A. Algozeeb, M.G. Stanford, C. Kittrell, W. Chen, R. V. Salvatierra, M. Ren, E.A. McHugh, P.A. Advincula, Z. Wang, M. Bhatt, H. Guo, V. Mancevski, R. Shahsavari, B.I. Yakobson, J.M. Tour, Gram-scale bottom-up flash graphene synthesis, Nature 577 (2020) 647–651, https://doi.org/10.1038/s41586-020-1938-0.

[35] Q. Dong, Y. Yao, S. Cheng, K. Alexopoulos, J. Gao, S. Srinivas, Y. Wang, Y. Pei, C. Zheng, A.H. Brozena, H. Zhao, X. Wang, H.E. Toraman, B. Yang, I.G. Kevrekidis, Y. Ju, D.G. Vlachos, D. Liu, L. Hu, Programmable heating and quenching for efficient thermochemical synthesis, Nature 605 (2022) 470–476, https://doi.org/10.1038/s41586-022-04568-6.

[36] J. Du, Y. Zhang, H. Lv, A. Chen, N/B-co-doped ordered mesoporous carbon spheres by ionothermal strategy for enhancing supercapacitor performance, J. Colloid Interface Sci. 587 (2021) 780–788, https://doi.org/10.1016/j.jcis.2020.11.037.

[37] Q. Wang, Q. Feng, Y. Lei, S. Tang, L. Xu, Y. Xiong, G. Fang, Y. Wang, P. Yang, J. Liu, W. Liu, X. Xiong, Quasi-solid-state Zn-air batteries with an atomically dispersed cobalt electrocatalyst and organohydrogel electrolyte, Nat. Commun. 13 (2022) 3689, https://doi.org/10.1038/s41467-022-31383-4.

[38] Y.-C. Wang, L. Huang, P. Zhang, Y.-T. Qiu, T. Sheng, Z.-Y. Zhou, G. Wang, J.-G. Liu, M. Rauf, Z.-Q. Gu, W.-T. Wu, S.-G. Sun, Constructing a triple-phase interface in micropores to boost performance of Fe/N/C catalysts for direct methanol fuel cells, ACS Energy Lett. 2 (2017) 645–650, https://doi.org/10.1021/acsenergylett.7b00071.

[39] H. Zhang, H.C. Chen, S. Feizpoor, L. Li, X. Zhang, X. Xu, Z. Zhuang, Z. Li, W. Hu, R. Snyders, D. Wang, C. Wang, Tailoring oxygen reduction reaction kinetics of Fe-N-C catalyst via spin manipulation for efficient zinc-air batteries, Adv. Mater. (2024) 2400523, https://doi.org/10.1002/adma.202400523.

[40] R. Zeng, Q. Gao, L. Xiao, W. Wang, Y. Gu, H. Huang, Y. Tan, D. Tang, S. Guo, Precise tuning of the d-band center of dual-atomic enzymes for catalytic therapy, J. Am. Chem. Soc. 146 (2024) 10023–10031, https://doi.org/10.1021/jacs.4c00791.

[41] T.-X. Huang, X. Cong, S.-S. Wu, K.-Q. Lin, X. Yao, Y.-H. He, J.-B. Wu, Y.-F. Bao, S.-C. Huang, X. Wang, P.-H. Tan, B. Ren, Probing the edge-related properties of atomically thin MoS_2 at nanoscale, Nat. Commun. 10 (2019) 5544, https://doi.org/10.1038/s41467-019-13486-7.

[42] P. Zhang, H.-C. Chen, H. Zhu, K. Chen, T. Li, Y. Zhao, J. Li, R. Hu, S. Huang, W. Zhu, Y. Liu, Y. Pan, Inter-site structural heterogeneity induction of single atom Fe catalysts for robust oxygen reduction, Nat. Commun. 15 (2024) 2062, https://doi.org/10.1038/s41467-024-46389-3.

[43] Y. Zhao, H.C. Chen, X. Ma, J. Li, Q. Yuan, P. Zhang, M. Wang, J. Li, M. Li, S. Wang, H. Guo, R. Hu, K.H. Tu, W. Zhu, X. Li, X. Yang, Y. Pan, Vacancy defects inductive effect of asymmetrically coordinated single-atom $Fe\text{-}N_3S_1$ active sites for robust electrocatalytic oxygen reduction with high turnover frequency and mass activity, Adv. Mater. 36 (2023) 2308243, https://doi.org/10.1002/adma.202308243.

[44] E. Zhu, T. Zheng, J. Yu, C. Shi, L. Zhou, H. Jin, J. Yang, G. Luo, D. Wei, X. Yang, M. Xu, Electron redistribution and proton transfer induced by atomically fully exposed Cu-O-Fe clusters coupled with single-atom sites for efficient oxygen electrocatalysis, Energy Storage Mater. 69 (2024) 103410, https://doi.org/10.1016/j.ensm.2024.103410.

[45] Q. Luo, Q. Ma, T. Liu, Y. Luo, L. Wang, C. Guo, L. Wang, Improving magnetic resonance imaging and chemodynamic therapy properties via tuning the Fe(ii)/Fe(iii) ratio in hydrophilic single-atom nanobowls, ACS Nano 18 (2024) 10063–10073, https://doi.org/10.1021/acsnano.3c12305.

[46] Z. Li, Z. Tian, H. Cheng, T. Wang, W. Zhang, Y. Lu, Y. Lai, G. He, Engineering d-band center of FeN_4 moieties for efficient oxygen reduction reaction electrocatalysts, Energy Storage Mater. 59 (2023) 102764, https://doi.org/10.1016/j.ensm.2023.04.003.

[47] L. Peng, J. Yang, Y. Yang, F. Qian, Q. Wang, D. Sun-Waterhouse, L. Shang, T. Zhang, G.I.N. Waterhouse, Mesopore-rich Fe-N-C catalyst with FeN_4-O-NC single-atom sites delivers remarkable oxygen reduction reaction performance in alkaline media, Adv. Mater. 34 (2022) 2202544, https://doi.org/10.1002/adma.202202544.

[48] J. Li, L. Jiao, E. Wegener, L.L. Richard, E. Liu, A. Zitolo, M.T. Sougrati, S. Mukerjee, Z. Zhao, Y. Huang, F. Yang, S. Zhong, H. Xu, A.J. Kropf, F. Jaouen, D.J. Myers, Q. Jia, Evolution pathway from iron compounds to Fe_1(II)-N_4 sites through gas-phase iron during pyrolysis, J. Am. Chem. Soc. 142 (2019) 1417–1423, https://doi.org/10.1021/jacs.9b11197.

[49] Y. Zhao, H. Wu, Y. Wang, L. Liu, W. Qin, S. Liu, J. Liu, Y. Qin, D. Zhang, A. Chu, B. Jia, X. Qu, M. Qin, Sulfur coordination engineering of molybdenum single-atom for dual-functional oxygen reduction/evolution catalysis, Energy Storage Mater. 50 (2022) 186–195, https://doi.org/10.1016/j.ensm.2022.05.015.

[50] J. Liu, W. Chen, S. Yuan, T. Liu, Q. Wang, High-coordination $Fe\text{-}N_4SP$ single-atom catalysts via the multi-shell synergistic effect for the enhanced oxygen reduction reaction of rechargeable Zn-air battery cathodes, Energy Environ. Mater. 17 (2024) 249–259, https://doi.org/10.1039/d3ee03183g.

[51] X. Xie, H. Peng, K. Sun, W. Li, A. Liang, G. Ma, Z. Lei, Y. Xu, A simultaneous modulation strategy to construct high dense and accessible $Co\text{-}N_4$ sites for promoting oxygen reduction reaction in Zn-air battery, Adv. Funct. Mater. (2024) 2316037, https://doi.org/10.1002/adfm.202316037.

[52] F. Lu, K. Fan, L. Cui, B. Li, Y. Yang, L. Zong, L. Wang, Engineering FeN_4 active sites onto nitrogen-rich carbon with tubular channels for enhanced oxygen reduction reaction performance, Appl. Catal. B Environ. 313 (2022) 121464, https://doi.org/10.1016/j.apcatb.2022.121464.

[53] C. Jin, H. Deng, J. Zhang, Y. Hao, J. Liu, Jagged carbon nanotubes from polyaniline: strain-driven high-performance for Zn-air battery, Chem. Eng. J. 434 (2022) 134617, https://doi.org/10.1016/j.cej.2022.134617.

[54] B. Ji, J. Gou, Y. Zheng, X. Pu, Y. Wang, P. Kidkhunthod, Y. Tang, Coordination chemistry of large-sized yttrium single-atom catalysts for oxygen reduction reaction, Adv. Mater. 35 (2023) 2300381, https://doi.org/10.1002/adma.202300381.

[55] Y. Liu, L. Zhou, S. Liu, S. Li, J. Zhou, X. Li, X. Chen, K. Sun, B. Li, J. Jiang, H. Pang, Fe, N-inducing interfacial electron redistribution in NiCo spinel on biomass-derived carbon for bi-functional oxygen conversion, Angew. Chem. Int. Ed. 63 (2024) e202319983, https://doi.org/10.1002/anie.202319983.

[56] S. Liu, M. Wang, X. Sun, N. Xu, J. Liu, Y. Wang, T. Qian, C. Yan, Facilitated oxygen chemisorption in heteroatom-doped carbon for improved oxygen reaction activity in all-solid-state zinc-air batteries, Adv. Mater. 30 (2017) 1704898, https://doi.org/10.1002/adma.201704898.

[57] X. Liu, J. Wang, P. Lv, Y. Zhang, J. Li, Q. Wei, Gel polymer electrolyte based on deep eutectic solvent in flexible Zn-air batteries enables dendrite-free Zn anode, Energy Storage Mater. 69 (2024) 103382, https://doi.org/10.1016/j.ensm.2024.103382.